

See discussions, stats, and author profiles for this publication at: <https://www.researchgate.net/publication/50302920>

Surface Sensitive Study To Determine the Reactivity of Soot with the Focus on the European Emission Standards IV and VI

ARTICLE in THE JOURNAL OF PHYSICAL CHEMISTRY A · MARCH 2011

Impact Factor: 2.69 · DOI: 10.1021/jp1088417 · Source: PubMed

CITATIONS

18

READS

34

9 AUTHORS, INCLUDING:



Dangsheng Su

Chinese Academy of Sciences

643 PUBLICATIONS 13,104 CITATIONS

[SEE PROFILE](#)



Reinhard Niessner

Technische Universität München

593 PUBLICATIONS 12,189 CITATIONS

[SEE PROFILE](#)

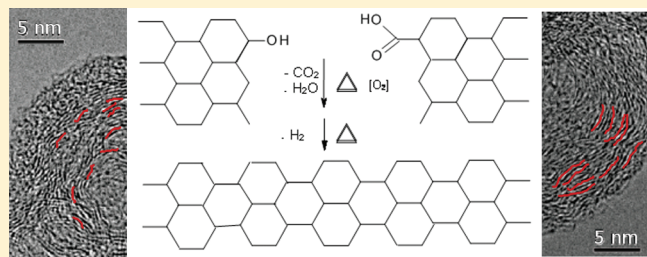
Surface Sensitive Study To Determine the Reactivity of Soot with the Focus on the European Emission Standards IV and VI

Manfred E. Schuster,[†] Michael Hävecker,[†] Rosa Arrigo,[†] Raoul Blume,[†] Markus Knauer,[‡] Natalia P. Ivleva,[‡] Dang Sheng Su,^{*,†} Reinhard Niessner,[‡] and Robert Schlögl[†]

[†]Department of Inorganic Chemistry, Fritz-Haber-Institut der Max-Planck-Gesellschaft, Faradayweg 4-6, D-14195 Berlin, Germany

[‡]Institute of Hydrochemistry, Chair for Analytical Chemistry, Technische Universität München, Marchioninistr. 17, D-81377 Munich, Germany

ABSTRACT: Diesel soot (Euro IV and Euro VI) was investigated with spectroscopic methods such as near-edge X-ray absorption fine structure (NEXAFS) spectroscopy and X-ray photoemission spectroscopy (XPS). C and O K-edge NEXAFS show that structural disorder on the surface is accompanied by a higher amount of oxygen functional groups. O K-edge NEXAFS and O1s XPS results are discussed with the aim to elucidate the nature of the oxygen surface species. The analysis of the data presented here allows the postulation of a hypothetical structure for soot samples emitted by diesel engines.



INTRODUCTION

Diesel exhaust soot particles (DESP) are considered one of the main cause of air pollution. In a recent study, the adverse effect of the increased air pollution on human health has been demonstrated.¹ Due to the complex composition of DESP, the mechanism of interaction of DESP with the human body is poorly understood. Recently it has been shown that soot particles produced under low-emission conditions exhibit a much higher toxic and inflammatory potential than particles from an old diesel engine operating under black smoke conditions.² This effect is assigned to the higher biological compatibility of the soot particles in the exhaust gases emitted by modern diesel engine operating under low-emission conditions characterized by small particles^{2,3} with highly defective surface structure. It is well-known that the reactivity of carbon materials is due to the presence of defects in the graphitic structure.⁴ By the same token, those defects are thought to interact with the human body. Thus, the detailed characterization of the surface structure of the soot particles^{5,6} is a crucial issue for understanding and predicting the potential risks of DESP for human health and for designing systems for soot treatment after the exhaust system.

Electron microscopy is one of the most suitable and applied technique to reveal structural features in carbon-related materials.^{7–9} Several high-resolution transmission electron microscopy (HRTEM) and electron energy loss spectroscopy (EELS)¹⁰ studies on soot samples have been reported focusing on the analysis of the nanostructure of soot particles with respect to the synthesis conditions (such as temperature, time, and initial fuel identity)¹¹ and the reactivity toward oxidation.^{9,12,13}

In our previous study,¹⁴ Raman EELS and HRTEM were used to characterize the structure of heavy-duty engine diesel soot

(Euro IV and Euro VI) samples and spark discharge (GfG) soot as obtained and oxidized and to correlate the structure with their reactivity toward oxidation.^{15,16}

HRTEM has shown that the soot samples contain, besides graphene basic structural units (BSUs), twisted ribbons with molecular units “sitting” on them. Katrinak et al.¹⁷ proposed, by observing the change of the π^*/σ^* ratio in the EELS of soot particles when the size of the soot particles changes, similar nanostructure for soot particles. Furthermore, in our previous study¹⁴ we have observed a different degree of disorder and a different amount of molecular carbon on the surface among the samples. Such a different nanostructure among the soot samples was indeed mirrored in different reactivity toward oxygen and in a different susceptibility toward structural modification induced by the oxidative treatment.

The Euro IV sample, for which changes in the bulk structure upon oxidation were observed, was shown to be less reactive upon oxidation compared to the Euro VI sample, which did not reveal significant structural changes in the bulk. Therefore knowledge about the surface composition is essential to explain the different behavior and reactivity of those samples.

Boosted by our previous investigations, in this work, the interest is focused on shading light on the surface chemical structure of the soot samples. Although, EELS offers spatial resolution and nearly single atom compositional sensitivity,¹⁸ the insensitivity of EELS for detecting oxygen functional groups such as carbonyl and carboxyl groups¹⁰ is the main disadvantage of this technique. In the present study, surface-sensitive techniques such

Received: September 16, 2010

Revised: January 12, 2011

Published: March 07, 2011

as NEXAFS and XPS are used to characterize the surface structure of the selected soot samples with the aim to get a complete picture about the nanostructure of the soot sample and its impact on the reactivity. Comparative NEXAFS and EELS studies have been carried out for the characterization of carbon materials over the past 2 decades,^{19,20} but soot particles have only been studied recently.^{21,22} Braun and co-workers^{10,22} have found a good agreement between EELS and NEXAFS results, although they pointed out that NEXAFS spectra show a higher amount of fine structures that cannot be resolved by EELS. Therefore, the combination of bulk (EELS) and surface-sensitive (XPS and NEXAFS) techniques is the best approach to obtain structural information about highly heterogeneously structured carbon material as soot samples.

C1s and O1s X-ray photoemission spectroscopy (XPS) was carried out at a synchrotron facility to reveal the chemical nature of the surface functional groups on the Euro IV, Euro VI, and GfG soot, and the spectra were compared to those of reference samples, such as HOPG, nanotubes (NC 3100), and lamp black (FL 101). The O K-edge NEXAFS spectra of the samples are correlated to the O1s XPS results. C K-edge NEXAFS spectroscopy was applied to reveal differences in the structural order of the surface carbon atoms. The characterization of the structure of the DESP and the susceptibility to structure modifications of the soot particles under specific reaction condition are the approaches used in this work to understand the reactivity of the soot particles. This study is useful for addressing specific thermochemical treatment of the exhaust gases aimed at reducing DESP emission and DESP toxicity.

■ EXPERIMENTAL SECTION

Materials. The Euro samples investigated in this work were generated under European Standard Emission norms IV and VI. They are referred to in the text as Euro IV and Euro VI. Euro IV was collected under World Harmonized Transient Cycle (WHTC) conditions from the undiluted raw exhaust of a heavy-duty test engine that fulfills Euro IV exhaust limits. Samples of Euro VI soot were taken under European Transient Cycle (ETC) conditions from the undiluted raw exhaust of a heavy-duty test engine that is designed to fulfill Euro VI exhaust limits. The soot samples were deposited on Bekipor Fecralloy metal fiber filter material (Bekaert, Belgium) with a fiber diameter of $\sim 10 \mu\text{m}$ and a filter diameter of 47 mm.

Graphite-like materials with different degrees of order were investigated as model systems: highly ordered pyrolytic graphite (HOPG) was used as reference for planar graphite with 100% sp^2 orientation, nanotubes (NC 3100) were used as the curved graphite structure model, and lamp black soot (Flammruss 101, Degussa) was used as highly fullerene-like model system.

To analyze the correlation between structural changes and reactivity of Euro VI and IV diesel soot and GfG soot, the samples were treated in a temperature range between 20 and 500 °C (heating rate 5 °C/min) with 5% oxygen in nitrogen. In the following text, the untreated samples will be referred to “as received” or “20” and the ones oxidized in 5% oxygen in nitrogen up to 773 K will be referred to as “oxidized” or “500”.

Characterization. XPS and NEXAFS experiments have been performed at the synchrotron radiation facility BESSY II (Berliner Elektronenspeicherringgesellschaft für Synchrotronstrahlung) using monochromatic radiation of the ISISS (Innovative Station for In Situ Spectroscopy) beamline as a tunable X-ray source.²³ Samples were transferred into the reaction cell, ~ 2 mm away

from an aperture to the differentially pumped stages of the lens system of the hemispherical analyzer (Phoibos 150, SPECS). Details of the setup are described elsewhere.²⁴ The excitation energy used for C1s/O1s core level spectra were 585/830 eV, respectively, resulting in a high surface sensitivity with an inelastic mean free path (IMFP) of the photoelectrons of about 0.86 nm. The spectra have been normalized to the impinging photon flux that has been determined by a cleaned Ag foil and corrected for the fraction of higher order as well as the electron current in the storage ring. Quantitative XPS data analysis was performed by using theoretical cross sections.²⁵

The O1s envelopes were fitted using mixed Gaussian–Lorentzian component profiles after subtraction of a Shirley background²⁶ using Casa XPS software.²⁷ For the spectra in which the species abundance was close to the detection limit, a linear background has been subtracted. The fitting was done by fixing the peak maximum within ± 0.1 eV for all spectra and applying a full width at half-maximum (fwhm) of 1.4–1.6 eV. The C1s envelopes were fitted as follows: the graphitic peak was fitted in an asymmetric peak, well-described by a Doniach–Sunjic model,²⁸ while the other peaks were fitted by using a mixed Gaussian–Lorentzian component profile after subtraction of a Shirley background. Atomic ratios were calculated using atomic sensitivity factors.²⁹ For all samples the XPS spectra were taken three times and the average of those measurements was used for analysis.

NEXAFS C and O K-edge spectra have been obtained in the Auger electron yield (AEY) mode by using the electron spectrometer as a detector. The kinetic energy window of the spectrometer has been set to 260–320 eV for C K-edge spectra and 520–560 eV for O K-edge spectra, respectively, and a pass energy of 50 eV has been applied. Simultaneously to the AEY spectra, a positively biased wire was used to obtain absorption spectra in the total electron yield mode (TEY). The monochromator was scanned in a continuous mode through the energy range of the C and O K-edge absorption edges; i.e., the monochromator was not swept in a stepwise manner for data acquisition but was driving with a constant speed, in this case 250 meV/s, without stopping for data retrieval. Data have been taken continuously, and the actual energy position at every data point was read back from the monochromator control. Raw spectra contained approximately 3000 data points. Typically, data reduction of a factor 4 was performed during analysis by averaging adjacent data points during data manipulation to increase the signal-to-noise ratio of the spectra. Absolute energy calibration has been done via the π^* resonance of TEY spectra of gas-phase O_2 at 530.9 eV^{30,31} and the second-order gas-phase O_2 at 265.45 eV. The spectral resolution was about 0.1 and 0.15 eV at the C and O K-edge, respectively. C K-edge raw spectra have been intensity normalized with a carbon-free Ag-foil. For all samples, the NEXAFS spectra were taken two times and the average of those measurements was used for analysis.

■ RESULTS

C1s XPS. Figure 1 reports the C1s spectra for the samples investigated and compared with C1s of HOPG taken as reference. The C1s of HOPG represents the line shape of almost pure, defect-free graphite measured as a standard with a line width that is mainly determined by the spectral resolution.³² The fitting of the main line has to be executed by use of an asymmetric model, which is best fit by a Doniach–Sunjic model.²⁸ The asymmetry is

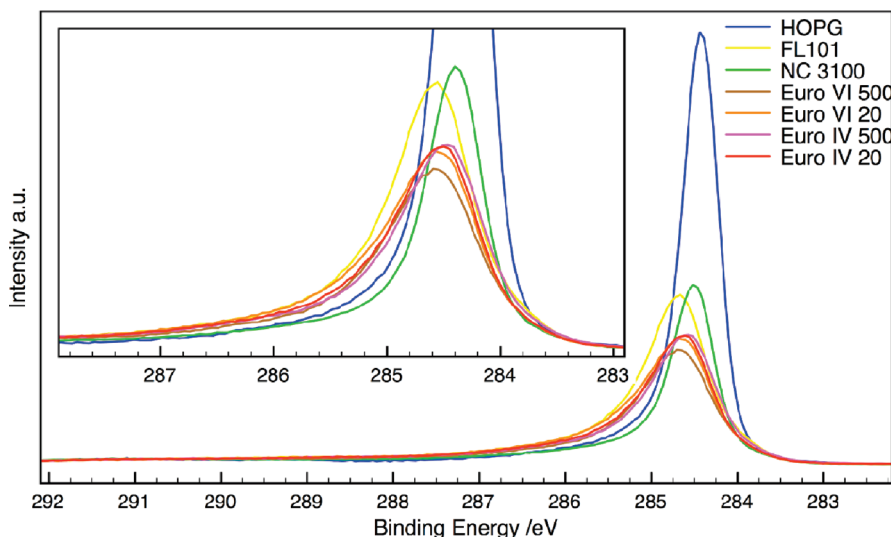


Figure 1. C1s XPS of HOPG, Flammruss 101, NC 3100, Euro IV, and Euro VI.

mainly due to the coupling of the core hole state created during the photoemission to the semimetallic valence band states of graphite and by the convolution of the primary photoemission with the phonon and plasmon loss spectra.^{33,34}

The influence of the defect structure on the absolute position of the main line and on the position of the shakeup at 291 eV has been discussed in literature.³⁵ To evaluate the difference in structural defectiveness among the samples, the C1s peaks have been normalized with respect to the shakeup at 291 eV. This is due to the fact that if any differences are present they are more pronounced on the main peak rather than in the shakeup.

With respect to the HOPG, all samples show a C1s peak with its maximum shifted to higher binding energy and have larger fwhm. Furthermore, a high intensity in the region between ~285 and ~291 eV is present. The latter features are attributed to oxygen functional groups.^{36,37}

The fitting of the C1s for carbon materials is not straightforward.

Literature reports a large variety of chemical shift values for carbon–oxygen for several carbon materials. Studies dealing with the characterization of the oxygenated species on the surface of carbon fibers show a very broad variation of O1s binding energies corresponding to a large variety of C–O bonding configurations.⁶⁷ Such a large variety of oxygen chemical bond configurations observed in the O1s does not correspond to comparable differences in the relative C1s. Obviously, the small concentration of defective states due to the different heteroatom configuration are masked by the overall carbon structure, leading to overlapping components in the high energy side.

For instance, plasmon satellite features occur at 5.6–7.2 eV in sp^2 carbons and at 11.3–12.5 eV in sp^3 carbon at higher BE than the main line,³⁸ which hinder the chemical shift identification^{39,40,35} of highly oxidized C–O functional groups. However, some tentative assignment in literature⁴ considers the features at 286.1 eV due to hydroxyl groups (C–OH), 287.6 eV due to carbonyl groups (C=O), and 289.1 eV due to ester groups [C=O(OR)].

In this work, the qualitative assignments of the components in C1s spectra are based on the following assumptions:⁴ for nearly defect free graphite the binding energy was found at around 284.6 eV,⁶¹ defective sp^2 and sp^3 C–C and C–H bonds give rise

Table 1. Full Width at Half-Maximum of the Main Peak in the C1s Spectra

sample	fwhm (eV)
HOPG	0.48
FL 101	0.85
NC 3100	0.57
Euro VI 500	0.9
Euro VI 20	1
Euro IV 500	0.95
Euro IV 20	0.97

to a C1s signal above 285 eV, and carbon heterobonds lead to a shift of the C1s component to higher binding energy. The more electronegative the heteroelement relative to carbon, the larger the chemical shift to higher binding energy.

Table 1 presents the fwhm for the main peak in the C1s spectra of the investigated samples. The value of 0.48 eV for HOPG is representing nearly defect free sp^2 hybridized carbon (284.6 eV) atoms. The value of 0.57 eV fwhm, as shown in Table 1, for the nanotube sample compared to 0.48 eV for HOPG indicates the high graphitization of this sample. However, the larger fwhm value can be assigned to contributions of sp^3 hybridized carbon/hydrocarbons sitting at a slightly higher binding energy (around 285.1 eV). Higher amounts of defects lead to a broader distribution of binding energies, which are then reflected in a broader line width. Therefore, the significantly higher values of the fwhm for the soot samples, between 0.85 and 1 eV, indicate a higher amount of defects/hydrocarbons in the structure. Defectiveness is also reflected in a decrease of the intensity of the main C1s peak. In contrast to HOPG, the soot samples present a more symmetric peak shape.

Difference spectra of the as received and the oxidized Euro VI sample (Figure 2, left side) indicate a loss of sp^2 hybridized carbon (284.4 eV) atoms with an additional loss of sp^3 states and oxygen functional groups, indicated by the positive signal between 285 and 287 eV. Therefore, the surface of the Euro VI sample undergoes modifications during the oxidation treatment described by a loss of the overall oxygen species (287 eV) and the loss of defective sp^2 and sp^3 states.

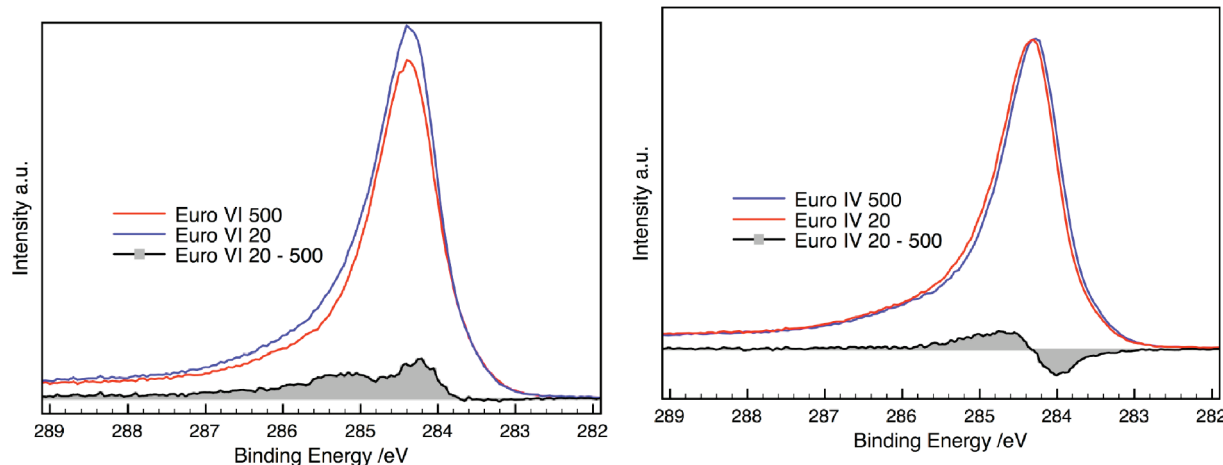


Figure 2. Difference spectra of the as received/oxidized Euro VI (left)/ Euro IV sample (right).

Table 2. Absolute Oxygen and Carbon Amount in Euro IV, Euro VI, NC 3100, and Flammruss 101

sample	% of oxygen	% of carbon
Euro IV 20	6.25	93.75
Euro IV 500	6.1	93.9
Euro VI 20	12.18	87.82
Euro VI 500	9.18	90.82
NC 3100	2.1	97.9
FL 101	6	94

The difference spectra of the as received and oxidized Euro IV sample reveal a different response to the oxidation treatment (Figure 2, right side). In particular, after the oxidation treatment the amount of sp^2 hybridized carbon increases together with a loss of defective sp^2 and sp^3 hybridized carbon atoms. This is also supported by the slight shift to lower binding energies of the main C1s peak of the oxidized Euro IV sample with respect to the as received one. This can be explained by a restructuring of the carbon atoms at the surface to increase the structural graphitic order of the Euro IV sample.

O1s XPS. The quantification of the oxygen to carbon ratio for the samples investigated is displayed in Table 2. It is shown that the heating and oxidation process leads to a reduction of the total amount of oxygen species in the soot samples. The NC 3100 sample has very low oxygen content, while the amount of oxygen in the FL 101 sample lies between the values for the nanotube and the soot samples.

Figure 3 shows the deconvoluted O1s spectra of the samples investigated. The fitting was executed considering energy positions and fwhm values presented in previous studies.^{41,42} Accordingly, the description of the O1s XP spectrum considers the following binding energy regions: 530.7 eV is assigned to a highly conjugated form of carbonyl oxygen, such as quinone groups;^{43,44} 531.1–531.8 eV is assigned to a carbon–oxygen double bond; 532.6 eV is the carbon–oxygen ether-like single bond; and 533.5 eV refers to the carbon–oxygen single bond in hydroxyl groups. The real position of water is under debate, but studies of adsorption of water carried out on polycrystalline graphite led to the identification of a very broad peak centered at 533 eV.⁴ The origin of a feature at 535.2 eV is not clearly identified; nevertheless, some authors assign it to adsorbed water and/or oxygen.

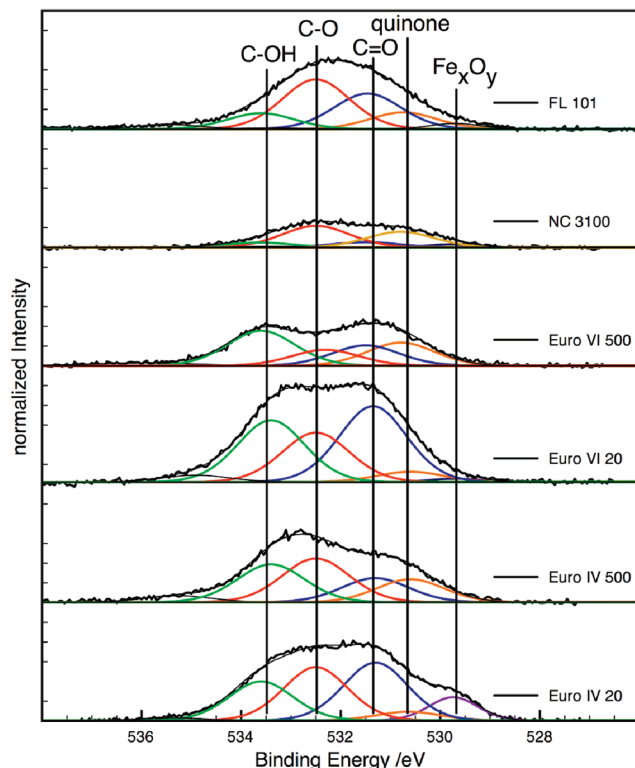


Figure 3. O1s XPS of Flammruss 101, NC 3100, GfG, Euro IV, and Euro VI.

Although the assignment of the components to a specific functional group is still under debate, qualitatively, the higher the electron density on the oxygen atom, the lower the binding energy. Therefore, the oxygen species with the lowest binding energy can be considered as an oxygen atom in a highly stabilized double chemical bonding configuration of the aromatic ring in the graphitic structure. Such a kind of defect leads to a localization of charge on the oxygen atom.

If such an oxygen species is adjacent to a more electronegative atom, its binding energy will be shifted to the higher binding energy side. Therefore, the binding energy distribution of the components can reflect the degree of oxidation of the carbon materials.

Table 3. Absolute Oxygen Abundance for the Individual Contributions in the Euro IV and Euro VI Samples

binding energy (eV)		Euro IV 20	Euro IV 500	Euro VI 20	Euro VI 500
529.8	Fe_xO_y	0.043	0.024	0.1495	0.192
530.6	quinone	0.044	0.319	0.22	0.835
531.4	$\text{C}=\text{O}$	1.56	1.456	4.072	2.458
532.5	$\text{C}-\text{O}$	1.623	1.374	3.052	2.131
533.7	$\text{C}-\text{OH}$	2.599	2.556	4.044	2.995
>534	absorbates	0.381	0.367	0.646	0.563

The quantification of the different components in the O1s and their evolution during oxidation is summarized in Table 3 for the investigated samples. For the Euro IV sample, a slight decrease of the contribution at 532.5 and 531.4 eV is observed upon oxidation. However, the most significant change observed for the Euro IV samples is the strong increase of the species at 530.6 eV. Therefore, $\text{C}-\text{O}$ and $\text{C}=\text{O}$ are partly converted to higher oxidation state species and mainly into the low binding energy component at 530.6 eV.

For the Euro VI samples, a similar trend is observed: the oxidation treatment reduces the oxygen species at 531.4, 532.5, and 533.7 eV while an increase of the contribution at 530.6 eV occurs. On the basis of these results, it is possible to assume that, during the oxidation treatment, the soot samples undergo two reaction pathways involving the oxygen species: the most probable dehydration reaction and thermal decomposition reduce the total amount of oxygen species and lead to the formation of the species at 530.6 eV, which consist of conjugated oxygen species. The oxygenated species already present can undergo further oxidation.

A similar behavior is observed for the Euro IV sample. However, no increase of the graphitization could be observed in the C1s of the Euro VI while an increase in the graphitization occurs for the Euro IV sample. Therefore, Euro IV undergoes a dehydrogenation reaction, possibly involving the conversion of the 531.4 eV species to the 530.6 eV species. The conversion of the 531.4 eV species to the 530.6 eV species implies the presence of radical dangling bonds in the benzene ring that can activate oxygen and form a quinone species. This may occur through direct conversion or through thermal decomposition of the species at 531.4 eV and successive oxygen insertion in the graphitic structure.

The peak at around 529.8 eV that is visible in the spectrum of Euro IV 20 and Euro VI 20 is assigned to Fe_xO_y . As already mentioned before, this feature is observed in this measurement as the soot sample does not uniformly cover the substrate which could be exposed, and therefore, a photoemission signal from the filter material, stainless steel, is also obtained.

In this work, photon-energy-dependent depth-profiling is used to determine the concentration profile of the subsurface oxygen species within the first few nanometers below the surface.⁴⁵ The measurements on the O1s and C1s ionization edge were performed with the aim to get information about the evolution of the composition of the oxygen functional groups in the samples due to different surface sensitivity.⁴⁶ By tuning the energy of the X-ray source, the kinetic energy⁴⁷ of the photo-emitting electrons can be increased. By using higher photon energy, contributions from deeper subsurface regions are obtained.

The evolution of the absolute oxygen amount and amount of the individual species present in the as received/oxidized Euro

Table 4. Absolute Oxygen Abundance Obtained by Depth Profile Measurements for Euro IV/VI as Received/Oxidized

sample	absolute oxygen abundance (%), surface → bulk		
	630/385 ^a	830/585 ^a	1030/785 ^a
Euro IV 20	12.7	6.3	5.5
Euro IV 500	15.4	6.1	5.2
Euro VI 20	21.7	12.2	11.2
Euro VI 500	19.4	9.2	8

^a E_{exc} (eV) O1s/C1s.

IV/VI samples is shown in Tables 4 and Table 5 as a function of the photon energy. The chemical composition of the surface and the near-surface region varies in a different way for the Euro IV and Euro VI samples. The as received Euro VI sample has nearly twice as much surface oxygen compared to the as received Euro IV sample. Table 4 shows that the oxygen content for the as received Euro VI sample decreases significantly with increasing photon energy. A change of the photon energy from 630/385 eV to 1030/785 eV reduces the absolute oxygen amount from 21.7% to 11.2%. The oxidation treatment leads to a slight decrease of the surface and subsurface oxygen species within the Euro VI sample. Table 5 reveals that this is due to a loss of $\text{C}=\text{O}$ and $\text{C}-\text{O}$ while quinone groups are formed.

The as received Euro IV sample show an oxygen amount of 12.7% decreasing to 5.5% going from surface to more subsurface sensitivity. After the oxidation treatment, the Euro IV sample shows higher oxygen content on the surface (15.4%) compared to the as received Euro IV sample. The amount of subsurface oxygen is the same for the as received and oxidized Euro IV sample. This slight increase of the total oxygen amount is mainly due to the formation of quinone groups, as presented in Table 5.

This indicates that the oxidation/heat treatment introduces a small amount of oxygen functional groups onto the surface of the Euro IV sample. For the oxidized Euro VI sample, significant changes compared to the as received Euro VI sample can be observed. The oxygen content of the oxidized sample drops from an initial value of 19.4% to 9.2% to 8% with increasing photon energy. In relation to the as received Euro VI sample, this represents a loss of ~30% of the subsurface oxygen. This means that the high subsurface oxygen content in the as received sample is removed during the oxidation treatment through dehydration and thermal decomposition of the oxygen species originally present.

Table 5 presents the distribution of the single oxygen species for the depth profile measurements. As already shown in Table 4, the Euro IV sample has a much lower oxygen content subsurface than on the surface. The dominant contributions for the as received Euro IV sample are $\text{C}=\text{O}$, $\text{C}-\text{O}$, and mainly $\text{C}-\text{OH}$ bonds. For the more bulk-sensitive measurements, those species

Table 5. Photon-Energy-Dependent Evolution of the Absolute Oxygen Abundance for the Individual Functional Groups in the Euro IV and Euro VI Samples

sample	photon energy (eV)	absolute oxygen abundance (%)				
		Fe_xO_y 529.7 eV	quinone 530.6 eV	$\text{C}=\text{O}$ 531.4 eV	$\text{C}-\text{O}$ 532.5 eV	$\text{C}-\text{OH}$ 533.7 eV
Euro IV 20	630/385	0.065	0.307	3.338	2.661	5.555
	830/585	0.043	0.044	1.56	1.623	2.599
	1030/785	0.0153	0.051	0.546	1.671	2.554
Euro IV 500	630/385	0.017	0.996	3.443	3.301	6.718
	830/585	0.024	0.319	1.456	1.374	2.556
	1030/785	0.022	0.151	0.993	1.309	2.437
Euro VI 20	630/385	0.236	0.333	7.59	4.569	7.707
	830/585	0.149	0.220	4.072	3.052	4.044
	1030/785	0.059	0.316	3.534	2.746	3.968
Euro VI 500	630/385	0.346	1.103	5.559	3.779	7.367
	830/585	0.192	0.835	2.458	2.131	2.995
	1030/785	0.127	0.213	2.406	1.721	2.975

decrease in intensity but remain the most significant ones with a stronger decrease for $\text{C}=\text{O}$ than for the other species.

The oxidized Euro IV sample shows that within the first $\sim 5 \text{ \AA}$ a significant increase of quinone-like species can be observed, while the amount of $\text{C}=\text{O}$ stays constant. Additionally, $\text{C}-\text{O}$ and $\text{C}-\text{OH}$ contributions increase but in a less pronounced way than the quinone-like species. Beside the formation of quinone-like species in the oxidized Euro IV sample, the evolution of the species for the more bulk sensitive measurements is consistent with the results obtained for the as received one.

As shown in Table 4, the amount of oxygen in the as received Euro VI sample is significantly higher than the one present in the as received Euro IV sample. While for the Euro VI 20 sample an amount of quinone-like species comparable to those in the Euro IV 20 sample is found, the percentage of $\text{C}=\text{O}$ and $\text{C}-\text{O}$ is nearly twice as high in the Euro VI 20 sample. This persists when measurements are more subsurface sensitive. Importantly, the species at $\sim 530.6 \text{ eV}$, assigned to conjugated $\text{C}=\text{O}$, such as quinone species, does not significantly decrease, which is in contrast to the data obtained for the Euro IV 20 sample. Those data indicate that the as received Euro VI sample is higher functionalized, due to the presence of quinone-like species, and parallel to that, a higher degree of oxidation states is present, due to higher contributions in the range of $\text{C}-\text{OH}$ species, than in the Euro IV 20 sample.

After the oxidation and heat treatment, the composition of species in the Euro VI sample is altered differently than for the Euro IV sample. A strong increase of the species at 530.6 eV is observed, while a significant loss of $\text{C}=\text{O}$ and $\text{C}-\text{O}$ functional groups can be observed. The amount of $\text{C}-\text{OH}$ groups is reduced more strongly in the subsurface than in the surface region.

The more significant increase of quinone-like species in the surface and subsurface region and the loss of $\text{C}-\text{OH}$ functional groups especially in the subsurface region in the Euro VI sample due to the oxidation process are the most significant and important differences to the Euro VI sample.

C K-Edge NEXAFS. Figure 4 shows C K-edge NEXAFS spectra of HOPG, GfG, NC, FL, Euro IV, and Euro VI. In order to analyze the structural differences in the NEXAFS spectra of the soot samples, it is necessary to describe the typical structural

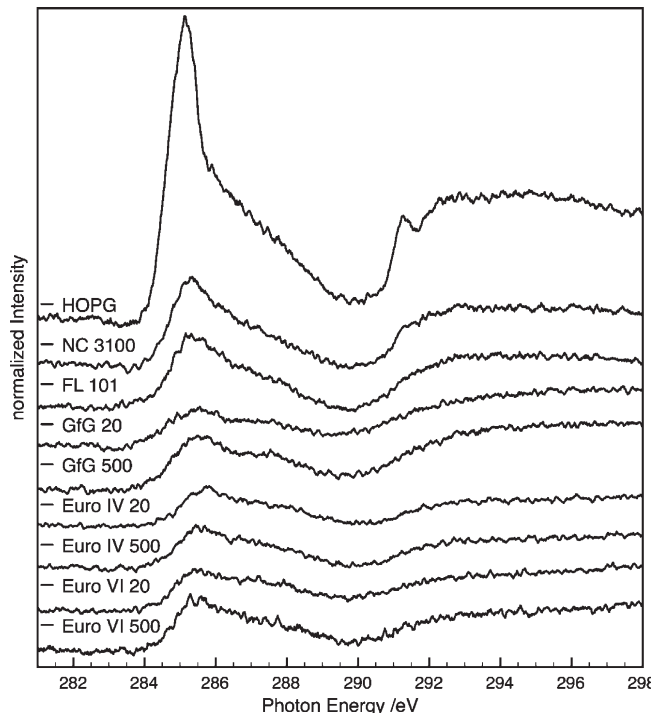


Figure 4. C K-edge NEXAFS of HOPG, Flammruss 101, NC 3100 GfG, Euro IV, and Euro VI.

features in the C K-edge NEXAFS for carbon materials reported in the literature. The C K-edge for graphite-like materials is composed of the π^* feature at around 285.6 eV and the σ^* feature at around 292 eV,^{48–50,61} originating mainly from the excitation to respectively the π^* antibonding and σ^* antibonding orbitals at the sp^2 ($\text{C}=\text{C}$ bond in the ring) site from the C1s level, respectively. Part of the spectrum area in the region assigned to σ^* states contains also contributions from extensions of the π^* continuum, which starts at around 282–287 eV. Assignment of the spectral features between 286 and 290 eV is quite controversial in the literature.^{51,53,56–58} Urquhart et al.⁵¹ assign the band at 286–287 eV to the C1s ($\text{C}-\text{R}$) \rightarrow $1\pi^* \text{C}=\text{C}$ transition that is characteristic for functionalized aromatic groups. In

analogy to functionalized oxygenated organic model compounds,^{52–54} the resonance peaks located at 286.8, 287.8, and 288.8 eV in the C K-edge NEXAFS spectrum of oxidized CNTs are assigned to $\text{C}1s \rightarrow \pi^*$ ($\text{C}=\text{O}$), $\text{C}1s \rightarrow \sigma^*$ ($\text{C}-\text{H}$), and $\text{C}1s \rightarrow \pi^*$ ($\text{O}=\text{C}-\text{OH}$ species) transitions, respectively.

Other studies⁵⁵ focused on the investigation of the structural features of C_{60} by NEXAFS consider the strong resonances at 286 and 288 eV in the C K-edge originating from $\text{C}1s \rightarrow \pi^*$ ($\text{C}=\text{C}$ in curved graphitic planes). Possible contamination of $\text{C}-\text{H}$ species on the surface that would give σ^* ($\text{C}-\text{H}$) transitions are also reported^{56,57} to be at about 288 eV. Moreover, small peaks in the area between 287 and 290 eV with a more distinct peak at 288.4 eV have been attributed to “interlayer states” caused by poor alignment between the graphene layers⁵⁸ of disrupted but pure graphite.

Structural features in the area 284–285 eV were observed by Entani et al.⁵⁹ and were explained in terms of edge-derived electronic states. According to the literature,⁵⁹ these states (E and E^*) originate from the edge states appearing at the zigzag edge of graphite. Despite the high structural heterogeneity of the defects sites occurring in commercial carbonaceous material, the resonances of those sites in the C K-edge NEXAFS spectra are close to each other and thus not easily resolvable.

Thus, due to different possible interpretation of the structural feature in the C K-edge NEXAFS spectrum for carbon material, the analysis of the structural features of a highly heterogeneous carbon system such as soot by means of NEXAFS cannot be approached, regardless of the knowledge of the surface nanostructure by means of HRTEM and XPS. As shown in Figure 4, all soot samples are characterized by a very broad resonance in the middle region between π^* and σ^* , which may indicate a broad surface state centered at the Fermi level and partially occupied. For comparison, HOPG, CNT, and FL C K-edge NEXAFS are reported in Figure 4. This allows a better understanding of how the C K-edge changes when the degree of order is gradually reduced from the highly structural ordered HOPG to CNT, where bending is introduced, and further to FL, where mismatching between graphene layer, functional groups, and non-aromatic domains are present.

The upper curve in Figure 4 shows HOPG (pure sp^2 hybridization). The $\text{1s} \rightarrow \pi^*$ resonance can be used as a fingerprint for sp^2 hybridized carbon atoms. The onset occurs at around 285 eV with a peak maximum at 285.6 eV. The $\text{1s} \rightarrow \sigma^*$ transitions occur above 291 eV excitation energy, which is in good agreement with the literature.^{60,61} The same sharp onset of the π^* feature is observed for NC 3100. The NC 3100 sample shows a first peak maximum at the lowest energy compared to the other investigated sample, with a maximum at around 0.3 eV below the π^* feature of the HOPG sample. These results are in agreement with those obtained by Chen et al.⁶² on MWNTs (15–20 nm in diameter). The authors explain the shift as a result of the weakening of the $\text{C}-\text{C}$ bonds due to the curvature of the graphene sheets and the larger interlayer spacing observed for the nanotube sample. Furthermore, the slightly higher fwhm of the $\text{C}1s$ peak observed for the MWCNT with respect to HOPG could indicate a shorter lifetime of the holes of $\text{C}1s$ in photo-emission compared to HOPG. The lamp black (FL 101) sample shows a less pronounced π state than the HOPG. According to the literature,⁶¹ the increased width of this resonance could indicate a splitting of the π states. The less intense and broader π^* resonance address for a splitting of π states indicates the high structural heterogeneity of the soot samples compared to pure

graphite. Therefore, deviations from the structural order of HOPG (considered as pure defect-free graphite) produce a decrease in the ratio of the π^*/σ^* signal, a shift of the π^* onset to lower BE, and broadening of the p^* resonance.

From C K NEXAFS analysis, GfG, FL 101, Euro IV and Euro VI samples are characterized by a surface layer of molecular carbon. This is revealed by the signals in the area at around 284 eV and further supported by HRTEM investigation¹⁴ on GfG, Euro IV and VI, and FL. Those measurements revealed the presence of molecular carbon sitting on top of the main particles. Thus, soot samples have a structure that resembles the structural order encountered in FL. Among the samples, Euro VI shows the sharpest π^* resonance at 285.6 eV and therefore a higher degree of sp^2 hybridized carbon. The features in the region 285–290 eV are clearly different among the investigated samples.

While the GfG sample presents a well-defined peak located at around 288 eV, a broad feature ranging from 285.5 to 286.5 eV characterizes the other samples. In particular, the Euro VI 20 sample has two peaks at around 287.5 and 288 eV. However, the origin of the feature at 287.5 is not yet clear. Those features are, however, correlated with the amount of oxygen species, as discussed in more detail in the next section.

The GfG and Euro VI samples show significantly different graphitic order, with higher structural order for the Euro VI than the GfG soot, as confirmed by the sharpness of the π^* resonance. This could be an indication that in the Euro VI the graphitic domains are interconnected by a chainlike fragment, containing oxygen species, while in the GfG sample similar oxygen species are present; however, the carbon structure present less aromatic character with a high amount of saturated (hydrogenated) $\text{C}-\text{C}$ bonds.

Those features at 287.5 and 288 eV are less significantly visible in the Euro VI sample oxidized up to 500 °C. In contrast, the onset of the tail of the π^* resonance is shifted to lower energies for the Euro IV 20 sample compared to Euro IV 500, thereby indicating a loss of molecular hydrocarbons during the oxidation process.

The difference method^{63,64} has been used for better comparison of the spectral shapes. The difference spectra between as obtained and oxidized Euro IV and Euro VI are plotted in Figure 5. In principle, the two plots must coincide if the samples show the same reactivity toward the oxidative treatment. The negative intensity in the π^* resonance indicates a higher hybridization of sp^2 -bonded carbon in the Euro VI 20 sample than in the Euro IV, also shown by a shift of the π^* peak maximum to lower binding energy for the Euro VI compared to Euro IV. Furthermore, a stronger presence of heteroatoms, assigned to carbon–oxygen bonds is present in the Euro VI sample compared to Euro IV.

The difference spectra of the oxidized samples reveal the same features in the region between 286 and 290 eV as for the as received samples but in a less pronounced way, indicating that the difference in carbon–oxygen bonds decreased. Additionally, it can be observed that the π^* peak maximum for the oxidized sample is at the same energy position, indicating that the structure of the two emission standard samples got more similar after the oxidation treatment.

The Euro IV sample after heating/oxidation treatment does not show substantial structural modifications, as shown by C K-edge NEXAFS in Figure 6a. The onset of the tail of the π^* resonance is shifted to slightly lower energies for the Euro IV 20 sample compared to Euro IV 500, as shown in the difference

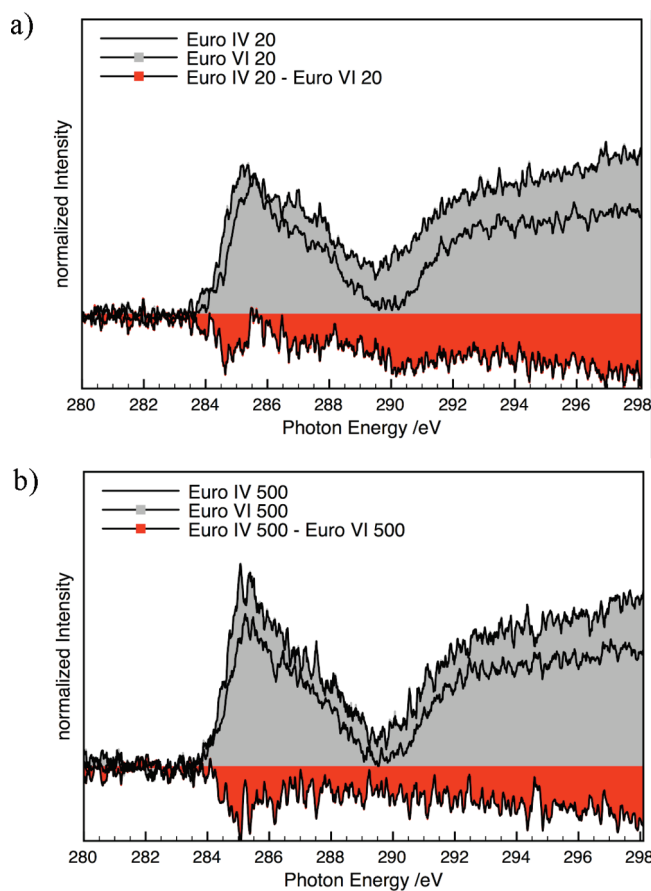


Figure 5. C K-edge NEXAFS difference spectra between Euro IV and Euro VI as received (a) and oxidized (b).

spectra (Figure 6a). The additional features assigned to oxygen functional groups and σ^* transitions do not undergo modifications during the oxidation treatment. Therefore, we can conclude that the changes in the features of the difference spectra of the Euro IV sample can be attributed to a slight increase of sp^2 hybridized carbon (~ 284.5 eV).

The two peaks at around 287.5 and 288 eV in the Euro VI 20 sample are less evident in the Euro VI sample oxidized up to 500 °C, as shown in Figure 6b. The Euro VI sample shows two more significant negative features between 284 and 285 eV in the difference spectra presented in Figure 6b parallel to positive features at ~ 286.5 and 287.2 eV. Those features would fit to an increase of the amount of sp^2 hybridized carbon atoms due to the oxidation process and a loss of defective states and oxygen functional groups during this process. Although the different intensities are very small compared to the signal-to-noise ratio, such interpretation fits with very well with the XPS analysis.

O K-Edge NEXAFS. The analysis of the structural features in the O K-edge NEXAFS of carbon is not well documented in the literature. Most of the published work was carried out on model compounds or they present a description of the O K-edge based on a phenomenological approach.

The resonance related to the $O1s \rightarrow \pi^*$ range for model compounds between 529.4 and 531.2 eV⁶⁵ depends on the nature of the C=O. In particular, for conjugated C=O double bond in an aromatic system such as benzoquinone, the resonance shift downward in energy to 529.4 eV.

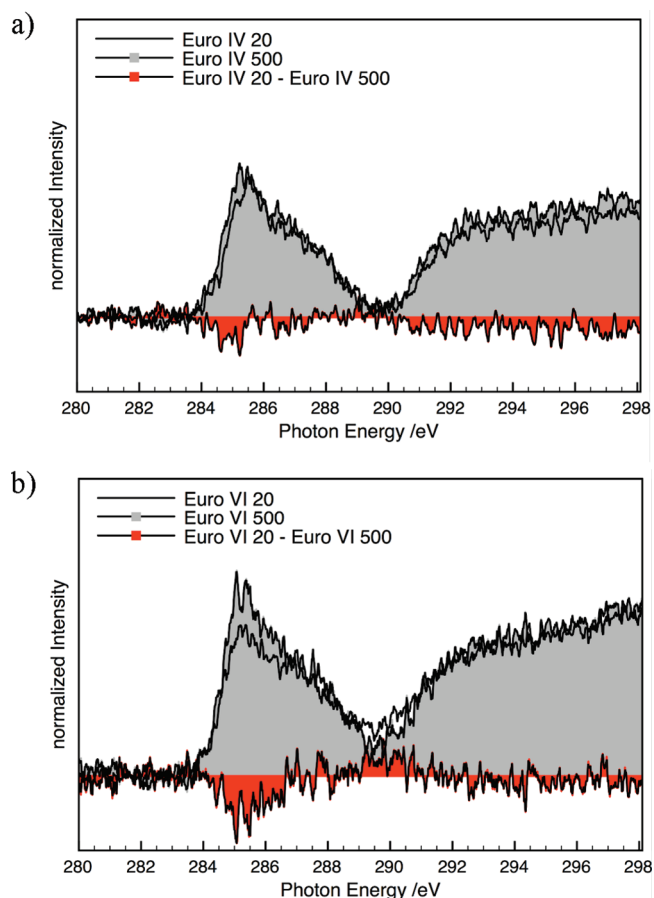


Figure 6. C K-edge NEXAFS difference spectra of the as received/oxidized Euro IV (a) and VI (b) soot sample.

If a C=O double bond is present close to another C=O double bond, a splitting of the π^* states is observed, which results in the generation of additional features in the O K-edge NEXAFS spectrum in the range between 533.1 and 533.9 eV.⁶⁵ The energy splitting between the two p^* states is smaller when the C=O is conjugated to another C=O double bond. According to the literature,⁵⁰ beside these two bands, another peak is observed below the ionization onset (>540 eV) between 535 and 538 eV due to the p transition.

More specifically, for carbon materials a peak at 533 eV is ascribed to the $O1s \rightarrow \pi^*$ excitation of a carboxylic group COO-.⁶⁶ The resonance at 533.6 eV is referred in the literature⁶⁷ to a carbonyl group attached to an alkyl chain. Furthermore, according to the experimental XPS measurements and theoretical work carried out on model compounds by Clark and co-workers,⁶⁸ the peak at 534.5 eV originates from $O1s \rightarrow \pi^*$ excitation of OH oxygen groups. The spectral intensity around 540 eV is composed of the σ^* resonance and the excitation to continuum¹⁹ and becomes larger with increasing numbers of oxygen atoms in a molecule.

Figure 7 reports the O1s NEXAFS spectra of the soot samples and reference samples. The intensities for the GfG samples are divided by a factor of 5 to fit the same intensity range as the other soot samples. This indicates the high oxygen content of the sample, which is also shown by the significant oxygen features in the C K-edge NEXAFS presented in Figure 4. Additionally, it is possible to evaluate that quite large variations in the O K-edge

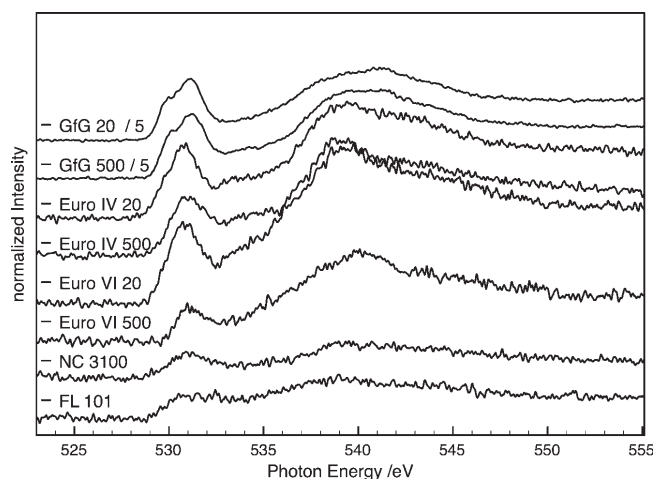


Figure 7. O K-edge NEXAFS of HOPG, Flammruss 101, NC 3100, GfG, Euro IV, and Euro VI.

have only a small effect on the C K-edge. The NC sample shows several spectral features, mainly dominated by a peak at 531 eV, assigned to C=O; a strong feature at 540; and higher energy losses, which are assigned to σ^* resonances. In contrast, the FL shows a lower π^*/σ^* ratio, which reflects a higher amount of oxygen in sp^3 bonding configuration. The area between those features shows a broader and less resolved feature compared to the NC sample, which reflects the presence of a more heterogeneous distribution of oxygen species. When compared with model compounds, the π^* fwhm is very broad for soot samples, which indicates that C=O double bonds are present in the sample in different chemical environments. According to Felicissimo et al.,⁶⁵ the presence of the bump between 532 and 538 eV indicates that the C=O double bonds are conjugated to each other.

The GfG sample shows a clear peak at 529.7 eV, which is well-assigned in the literature to iron oxides species.⁶⁹ Fe2p XPS measurements have revealed the presence of iron in our measurements, which originates from the supported Fe-mesh. Such a feature is present in almost all of the samples with an intensity that depends on the coverage of the soot on the supporting mesh. Another resonance at around 531 eV, due to carbon–oxygen double bond, is visible. This feature is more pronounced in the GfG sample than in the Euro samples.

The comparison between the as received and oxidized samples is helpful for the determination of single species in this broad resonance.

Figure 8 a displays the O K-edge NEXAFS for the Euro IV sample before and after oxidation treatment. The difference in intensities between the as received and oxidized sample is shown by the “red filled” curve, labeled as “Euro IV 20–Euro IV 500”. The difference spectra in Figure 8 a reveal no significant changes in the oxygen content and distribution of species as a result of the oxidation and heat treatment. The two more significant features in the difference spectrum are those located at 529.7 and 530.6 eV. The feature below 530 eV is a result of the sharpening of the peak at 530.6 eV after the oxidation treatment, which is probably due to the fact that the peak at 530.6 eV for the as received sample is not only due to oxygen–carbon bonds but also contains signal contributions from the support. Such a Fe_xO_y signal would be positioned at 529.7 eV and would explain this difference in the spectrum before and after the treatment. The positive feature at

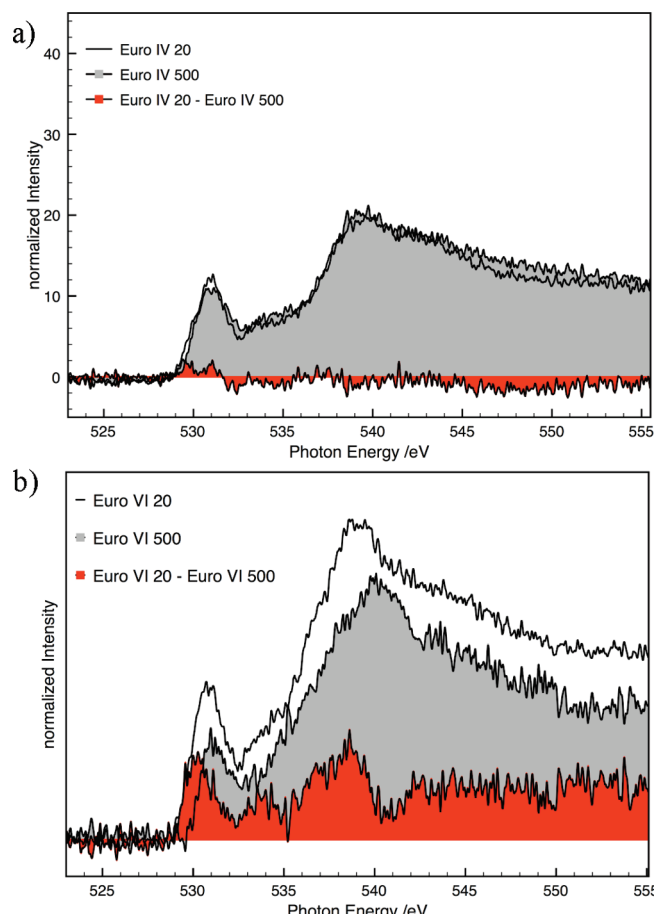


Figure 8. O K-edge NEXAFS difference spectra for untreated/treated Euro IV (a) and Euro VI (b) samples.

530.6 eV can be attributed to increase in the C=O double bond amount.

The changes in the O K-edge NEXAFS for the Euro VI sample are shown in Figure 8 b. Already at first glance, it is obvious that the Euro VI sample undergoes significant changes due to the oxidation treatment, which differs significantly from the Euro IV sample, which has no striking changes in the nature of the oxygen species resonances. The spectra presented in Figure 8 b show that the Euro VI sample loses a significant amount of its oxygen due to the oxidation and heat treatment. A loss of features located at around 530, 531.5, 534, 537, and 539 eV is observed. The difference at 530 eV could be due to Fe_xO_y contributions that are present in different amounts in both samples; however, the peak may also be due to pyrone/quinone oxygen groups. The positive signal observed at 531.5 eV is assigned to a loss of C=O species. The features at higher energy are associated with a splitting of π states (534 eV) that occur for conjugated C=O double bonds, while the latter features are assigned to σ transitions.⁶⁵

The significant differences in the oxygen content and distribution between the Euro IV and Euro VI samples can be additionally shown by a direct comparison between the as received/oxidized Euro IV and Euro VI samples. Those difference spectra are displayed in Figure 9. The difference spectra in the case of the fresh samples are displayed without filling, while the differences between Euro IV and VI after oxidation treatment are shown with a gray filling.

The intense negative features reveal the significantly higher oxygen content of the as received Euro VI sample in comparison

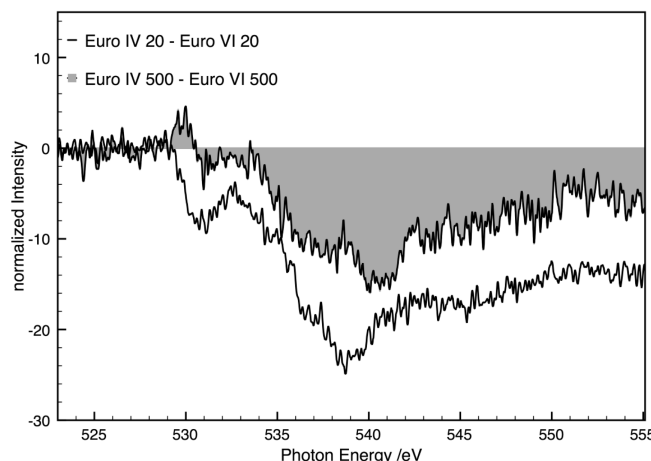


Figure 9. O K-edge NEXAFS difference spectrum for as received Euro IV and Euro VI samples overlaid with the difference spectrum for the oxidized Euro IV and VI samples.

to the Euro IV sample. It is also possible to determine features that are in a much higher amount present in the Euro VI sample, such as the ones at a photon energy of 531–531.5, 534, 536.5, and 539 eV. The second peak located at 531.2 eV is assigned to C=O in a graphitic structure, while features in the region of 533.5 eV are attributed to carbonyl groups attached to an alkyl chain. We assign the peak at 535 eV to an increase of C—OH bonds.

After the oxidation treatment the difference spectrum of Euro IV and VI shows still significant negative intensities above 534 eV. By analyzing the difference spectra for the Euro IV sample (Figure 8 a), Euro VI sample (Figure 8 b), and Euro IV minus Euro VI (Figure 9), it is clear that the amount of oxygen within the Euro VI sample decreases significantly while the amount and distribution for the Euro IV sample does not undergo remarkable changes.

The differences in the species at around 531.2 eV get significantly reduced during the oxidation treatment, leaving a slightly higher amount of this species on the Euro VI sample than on the Euro IV sample. A strong decrease of the relative amount of species between 536 and 540 eV can be observed for the oxidized Euro VI sample compared to Euro IV. This difference spectrum lets us identify another species located at 540 eV that is usually assigned to σ transitions.

Those features in the difference spectra gives information about five species present in the Euro VI sample. As NEXAFS does not suffer from any charging or chemical shift, these energy values can be used for the fitting of the O1s XPS.

The conclusions drawn from these difference spectra are that the Euro IV sample seems to contain less species at higher energies than the Euro VI sample. It is obvious that the O K NEXAFS spectrum changes significantly for the Euro VI sample before and after the oxidation and heat treatment. Those spectra (Figure 8 b) reveal that the oxygen content on the Euro VI sample gets significantly removed during the oxidation treatment, which is in contrast to the Euro IV sample (Figure 8 a), which does not seem to lose a remarkable amount of oxygen during the oxidation treatment.

This indicates that the Euro VI sample is much more accessible to modifications than the Euro IV sample, which seems to present some “inertness” to the heat and oxidation treatment.

Comparative Analysis of the Nanostructure of Euro IV and Euro VI. The structural variations due to the oxidation treatment are visible in the C1s XPS (Figure 1) spectra. For the Euro IV sample, an increase in the structural graphitic order can be associated with the increase of the signal at around 284.6 eV in the oxidized sample (Euro IV 500) with a simultaneous loss of defective sp^2/sp^3 states at around 285 eV. This is consistent with statistical curvature measurements on HRTEM micrographs and EELS measurements in a previous study. It was shown in this work that the Euro IV sample undergoes an increase in structural order during the oxidation treatment.

The C K-edge NEXAFS analysis of the Euro IV sample shows an increase of the intensity of the resonance at 285 eV after oxidation, which can be attributed to sp^2 hybridized carbon atoms. In addition, we observe a decrease of the σ^* resonance signal, which is associated to a loss of sp^3 hybridized carbon atoms. The loss of sp^3 carbon species and the decrease of the signal below 285 eV are consistent with the burning of molecular carbon, located on the surface of the soot particles, during oxidation that was observed also by means of HRTEM in a previous work.

The XPS C1s analysis of the Euro VI sample reveals a loss of defective sp^2/sp^3 carbons (285 eV) and a loss of oxygen functional groups (>285 eV). Although with a lower resolution, this is also observed in the C K-edge NEXAFS spectra of this sample as loss of structural features in the region between 286 and 288 eV.

The different sharpness of the π^* resonance in the NEXAFS C K spectra shows the stronger graphitic order for the Euro VI compared to the Euro IV sample. This is a general result from all the characterization techniques used in this and a previous work.¹⁴ Apparently, C1s XPS and C K NEXAFS also reveal a stronger feature in the region assigned to carbon heteroatom species for the Euro VI compared to Euro IV soot.

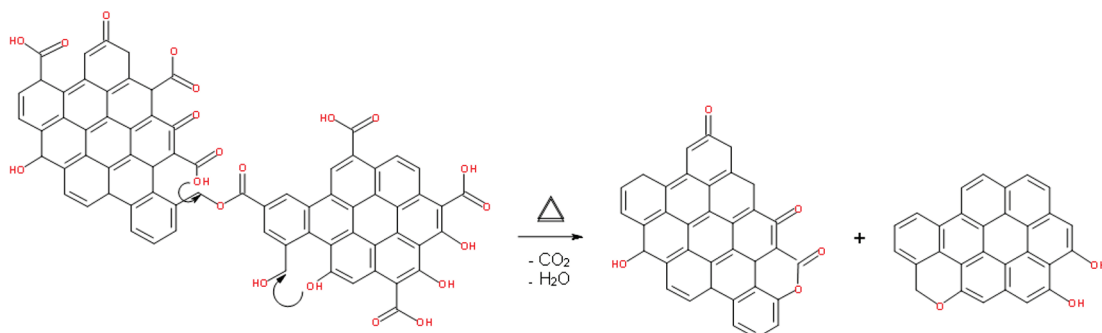
O1s XPS data reveal a higher concentration of surface and subsurface oxygen for the as received Euro VI than for the Euro IV sample. Both samples show that the subsurface contains approximately 50% less subsurface oxygen compared to the surface.

Upon oxidation Euro VI loses oxygen, which is more pronounced in the subsurface than in the surface region. In contrast, the Euro IV sample shows a similar amount of subsurface oxygen upon oxidation, while surface oxygen enrichment can be observed.

For the Euro IV sample, we observe an increase of surface C—O and C—OH species and a strong increase of the species at 530.7 eV (quinone-like oxygen species). This is explained as the generation of additional C=O double bonds in close proximity to the originally present C=O double bonds (531.7) in a conjugated double bond chemical configuration (quinone-like configuration).

The difference spectra method allows more specific information from the O K NEXAFS spectra to be obtained. A clear difference between Euro IV and Euro VI samples can be seen. The Euro VI sample contains more C=O, C—O, and C—OH contributions than the Euro IV sample but a similar amount of quinone groups. In conclusion, the depth profile measurements indicate that the Euro VI sample is highly oxidized and undergoes a significant reduction in its oxygen content due to the oxidation/heating treatment, whereas the lower oxygen content of the Euro IV sample is slightly enriched during the oxidation treatment.

The results obtained by the characterization techniques applied in this work, XPS and NEXAFS, are complementary to those obtained by HRTEM, EELS, and Raman¹⁴ for the understanding

Scheme 1. Reaction Scheme for the Euro VI Sample^a

^a Double bonds in the graphene domains are introduced randomly in the sketch in order to take the presence of saturated bonds into account.

of the structure of soot particles. The combination of the results obtained in this work with the knowledge about the bulk composition of those samples already obtained in a previous study¹⁴ is essential in order to subsequently propose a reaction scheme and a hypothetical model for the structure of Euro IV and Euro VI.

The “porosity” of the GfG sample, which is a result of the chain-like “structure”, facilitates a fast oxidation/combustion process. In contrast, no such “porosity” could be observed for the Euro samples. A “core–shell particle concept” with the particles having an “onionlike”¹⁴ structure can be assumed for the Euro particles. The result of the study undertaken here makes it possible to conclude that the oxidation/combustion process occurs from the outside to the inside of the soot particles. Such a combustion process is slowed down by the structure of the particles. This shell by shell “burning” fits with the particle size measurements¹⁴ that show a narrowing of the Euro IV particle size after the oxidation treatment. This can be explained by the removal of outer “shells”. Parallel to that, the carbon atoms inside the particle concomitantly rearrange themselves and increase their structural order.

The Euro VI sample does not undergo changes in the particle size distribution, which would mean in the core–shell particle concept that the outer shell hinders the oxidation/combustion treatment. This would mean that the particles are not combusted at all, or if combustion starts, the Euro VI particles combust completely, due to the higher reactivity and heterogeneity of oxygen functional groups in the Euro VI sample than in the Euro IV sample.

Such a high amount of oxygen species heterogeneous in nature and therefore in reactivity might lead to decomposition and oxidation, which would explain the complete combustion. Important to mention is the fact that the Euro VI sample does not only reduce the oxygen content but it changes the distribution of functional groups. Less stable oxygen groups are removed during the oxidation treatment or converted into more stable ones, as shown by the depth profile study.

On the basis of those experimental results, we can draw a structural model and a reaction scheme for the Euro samples: The Euro VI sample consists of a highly graphitic core with a highly oxidized surface. This can be due to the fact that the temperature in the engine was higher and therefore the carbon not exposed to oxygen is graphitized and carbon exposed to oxygen gets highly functionalized. The Euro IV sample was probably oxidized at lower temperature and therefore more molecular carbon is present. This leads to more changes in the

bulk during heating. This is supported by NEXAFS features located at 290 eV, which are more pronounced than in the Euro VI sample, indicating more hydrocarbons in the Euro VI, and by oxygen difference spectra. Moreover, depth profiling proves the highly functionalized and reactive surface of the Euro VI samples.

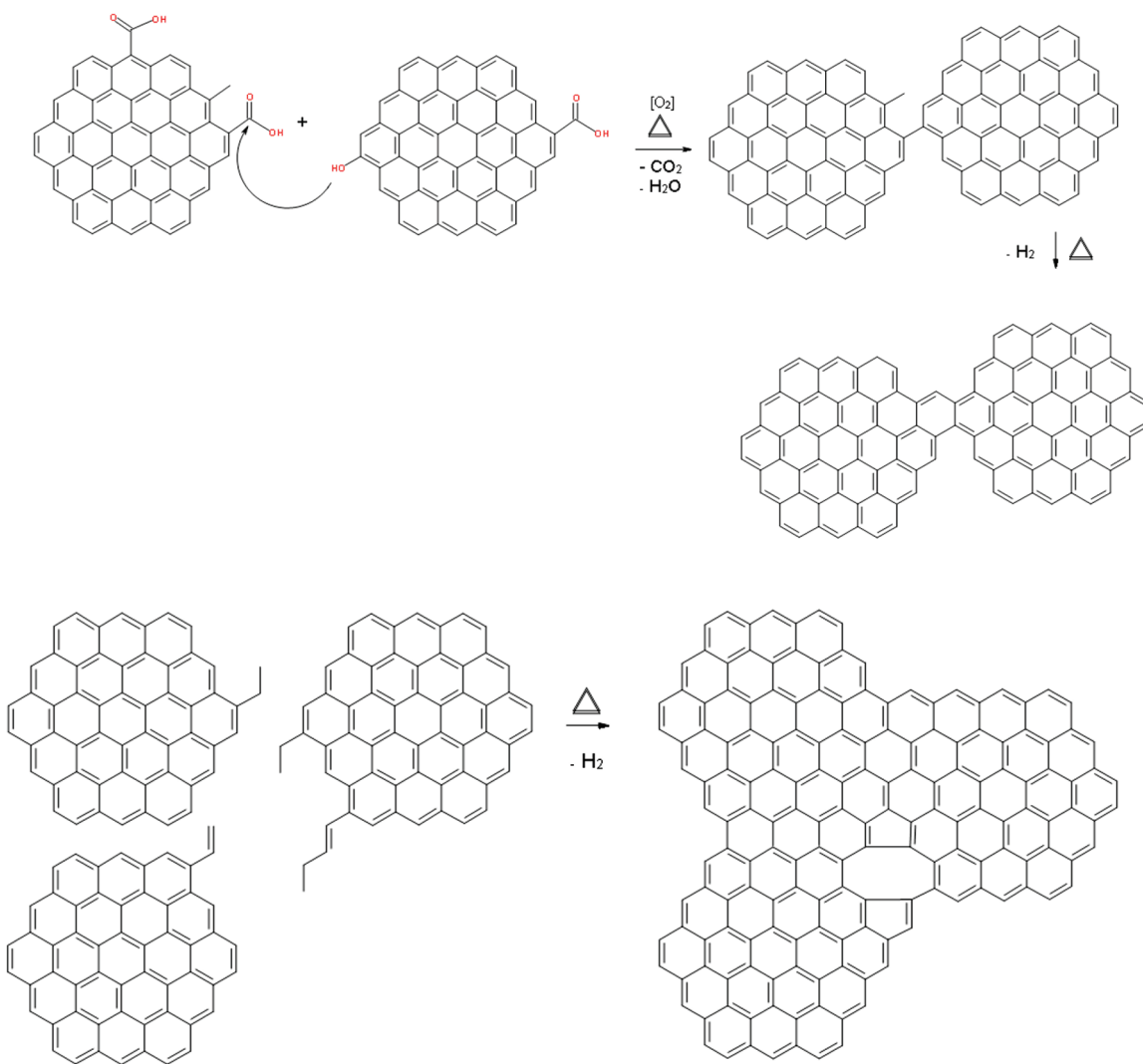
Euro VI Reaction Scheme. For the Euro VI sample, we assume a reaction during the oxidation treatment as displayed in Scheme 1. Due to the fact that we have more bending, higher oxygen content, and longer graphene fragments in the Euro VI sample, we can assume that the graphene fragments are decorated by oxygen species with lower thermal stability (species at higher binding energy). These graphene fragments are interconnected by an “oxygen bridge”.

During the oxidation treatment, the higher oxygen content of these species favors the complete combustion of the particles in the outer part of the soot agglomerates. Considering that we have an oxygen gradient, we can assume that we have for the outside particles an oxygen-rich atmosphere while inside the agglomerates a reducing atmosphere is present. Therefore, the particles inside undergo condensation and thermal decomposition of oxygen species. Considering the high oxygen content of this sample, the probability of neighboring oxygen species is very high. Therefore, intramolecular condensation reactions may occur. This fits perfectly with the shortening of the fiber length measured by HRTEM analysis, where an average fiber length of 2 nm is reduced to around 1 nm.

The occurrence of condensation reaction is supported by the modification of the distribution of the oxygen species observed by O1s XPS. The nature of the oxygen species is changed as H₂O and CO₂ is lost while quinone groups are formed. The more stable oxygen groups are formed while less stable ones are removed or converted into more thermal stable ones.

Euro IV Reaction Scheme. For the Euro IV sample a different reaction scheme is assumed, as shown in Scheme 2. The graphitic segments are characterized by lower oxygen content. This means that quite probably those graphene clusters are not interconnected by an oxygen bridge, as indicated by the lower curvature. The lower oxygen content and the observation of the growing of the graphene fragment lengths suggests the possibility of intermolecular condensation occurring. In the inner shell of the particles, intermolecular dehydrocyclization⁷⁰ between different graphene domains occurs, leading to the increase of the graphene domain size.

The molecular carbon units located on the surface are preferentially removed during oxidation. In the subsurface, where the O₂ concentration is limited by the diffusion regime of the

Scheme 2. Reaction Scheme for the Euro IV Sample

combustion process, the dehydration reaction and thermal decomposition of the oxygen species are favored.

The low oxygen content suppresses the complete combustion of the particles and favors thermal condensation of the core. The surface after the oxidation treatment is slightly enriched with oxygen species, which would be the precursor state of further oxidation. In addition, for the Euro IV sample there is a higher content of saturated carbon bonds that undergo oxidative dehydrogenation during the thermo-oxidative treatment. This would be an earlier step to the following oxidation of the carbon through the introduction of oxygen species.

These two intramolecular and intermolecular condensation pathways and the dehydrogenation of saturated C–C bonds are not exclusive for either sample; however, the study undertaken reveals that there is a preferential reaction pathway under thermo-oxidative conditions for either Euro IV or VI.

The GfG sample has a poorly graphic order with respect to the Euro samples and undergoes extensive structural changes during the heating treatment. This can be explained by the poor structural order and the high amount of oxygen in the sample, which lead during the heat treatment to a significant reordering.

■ CONCLUSION

X-ray photoelectron spectroscopy and near-edge X-ray absorption fine structure spectroscopy were used in this work to study the structure of soot particles.

It was possible to propose a hypothetical model for the structure of Euro IV and Euro VI soot and for their growing conditions on the basis of the results presented and discussed in this paper and a previous work.¹⁴ Despite the small differences in the C K-edge NEXAFS and C1s XPS features, the O K-edge and O1s spectra reveal significant differences in the nature and content of oxygen species. In particular, the Euro VI contains more oxygen species and those species undergo significant modifications under oxidation treatment, while in the Euro IV sample the oxygen content is lower but does not change significantly due to the oxidation treatment.

Furthermore, the reaction scheme proposed in this work explains the modifications observed and makes it possible to understand the difference in reactivity for the Euro IV and Euro VI soot sample. It can be clearly concluded from this study that the Euro VI sample is significantly more reactive than the Euro IV sample, and this environmental accessibility makes it potentially harmful.

■ AUTHOR INFORMATION

Corresponding Author

*Tel: +49 30 4648 5406. Fax: +49 30 4648 4405. E-mail: dangsheng@fhi-berlin.mpg.de.

■ REFERENCES

- (1) Sydbom, A.; Blomberg, A.; Parnia, S.; Stenfors, N.; Sandström, T.; Dahlén, S.-E. *Eur. Respir. J.* **2001**, *17*, 733.
- (2) Su, D. S.; Serafino, A.; Müller, J. O.; Jentoft, R. E.; Schlägl, R.; Fiorito, S. *Environ. Sci. Technol.* **2008**, *42*, 1761.
- (3) Su, D. S.; Jentoft, R. E.; Müller, J.-O.; Rothe, D.; Jacob, E.; Simpson, C. D.; Tomovic, Z.; Müllen, K.; Messerer, A.; Pöschl, U.; Niessner, R.; Schlägl, R. *Catal. Today* **2004**, *90*, 127.
- (4) Schlägl, R. *Handbook of Heterogeneous Catalysis*; Wiley: New York, 1997; Vol 1, 2.3.15, p 357.
- (5) Müller, J.; Su, D. S.; Jentoft, R. E.; Wild, U.; Schlägl, R. *Environ. Sci. Technol.* **2006**, *40*, 1231–1236.
- (6) Müller, J.-O.; Su, D. S.; Wild, U.; Schlägl, R. *Phys. Chem. Chem. Phys.* **2007**, *9*, 4018.
- (7) Palotás, Á. B.; Rainey, L. C.; Feldermann, C. J.; Sarofim, A. F.; Vander Sande, J. B. *Microsc. Res. Tech.* **1996**, *33*, 266.
- (8) Vander Wal, R. L.; Tomasek, A. J. *Combust. Flame* **2003**, *134*, 1.
- (9) Boehman, A. L.; Song, J.; Alam, M. *Energy Fuels* **2005**, *19*, 1857.
- (10) Braun, A.; Huggins, F. E.; Shah, N.; Chen, Y.; Wirick, S.; Mun, S. B.; Jacobsen, C.; Huffman, G. P. *Carbon* **2005**, *43*, 117.
- (11) Palotás, Á. B.; Rainey, L. C.; Feldermann, C. J.; Sarofim, A. F.; Vander Sande, J. B. *Microsc. Res. Tech.* **1996**, *33*, 266.
- (12) Vander Wal, R. L.; Tomasek, A. J. *Combust. Flame* **2003**, *134*, 1.
- (13) Vander Wal, R. L.; Yezerets, A.; Currier, N. W.; Kim, D. H.; Wang, C. M. *Carbon* **2007**, *45*, 70.
- (14) Knauer, M.; Schuster, M. E.; Su, D. S.; Schlägl, R.; Niessner, R.; Ivleva, N. P. *J. Phys. Chem. A* **2009**, *113*, 13871–13880.
- (15) Ivleva, N. P.; Messerer, A.; Yang, X.; Niessner, R.; Pöschl, U. *Environ. Sci. Technol.* **2007**, *41*, 3702.
- (16) Knauer, M.; Carrara, M.; Rothe, D.; Niessner, R.; Ivleva, N. P. *Aerosol Sci. Technol.* **2009**, *43*, 1.
- (17) Katrinak, K. A.; Rez, P.; Buseck, P. R. *Environ. Sci. Technol.* **1992**, *26*, 1967.
- (18) Browning, N. D.; Wallis, D. J.; Nellist, P. D.; Pennycook, S. J. *Micron* **1997**, *28*, 333.
- (19) Stöhr, J. *NEXAFS Spectroscopy*; Springer Series in Surface Science; Springer Verlag: Berlin, 1996; p 25.
- (20) Rightor, E. G.; Hitchcock, A. P.; Ade, H.; Leapman, R. D.; Urquhart, S. G.; Smith, A. P.; Mitchell, G.; Fischer, D.; Shin, H. J.; Warwick, T. *J. Phys. Chem. B* **1997**, *101*, 1950.
- (21) Braun, A. *J. Environ. Monitor.* **2005**, *7*, 1059–1065.
- (22) Braun, A.; Kubativa, A.; Wirick, S.; Mun, S. B. *J. Electron Spectrosc. Relat. Phenom.* **2009**, *170*, 42.
- (23) M. Hävecker, Senf, F.; Schmidt, J.-S.; A. Knop-Gericke, Eberhardt, W.; R. Schlägl, to be submitted to *Nucl. Instr. Methods*
- (24) Vass, E. M.; Hävecker, M.; Zafeiratos, S.; Teschner, D.; Knop-Gericke, A.; Schlägl, R. *J. Phys.: Condens. Matter* **2008**, *20*, 1.
- (25) Yeh, J. J.; Lindau, I. *Atomic Data Nucl. Tables* **1985**, *32*, 1.
- (26) Shirley, D. A. *Phys. Rev. B* **1972**, *5*, 4709.
- (27) CasaXPS software.
- (28) Wertheim, G. K.; Citrin, P. H. *Photoemission in Solids I*; Springer Verlag: Berlin, 1979; p 197.
- (29) Briggs, D.; Seah, M. P. *Practical Surface Analysis*; Wiley: Chichester, 1990.
- (30) Ma, Y.; Chen, C. T.; Meigs, G.; Randall, K.; Sette, F. *Phys. Rev. A* **1991**, *44*, 1848.
- (31) Hitchcock, A. P.; Brion, C. E. *J. Electron Spectrosc. Relat. Phenom.* **1980**, *18*, 1.
- (32) Prince, K. C.; Ulrych, I.; Peloi, M.; Ressel, B.; Cháb, V.; Crotti, C.; Comicioli, C. *Phys. Rev. B* **2000**, *62*, 6866.
- (33) Baer, Y. *J. Electron Spectrosc. Relat. Phenom.* **1981**, *24*, 95.
- (34) van Attekum, P. M. T. M.; Wertheim, G. K. *Phys. Rev. Lett.* **1979**, *43*, 1896.
- (35) Schlägl, R.; Boehm, H. P. *Carbon* **1983**, *21*, 345.
- (36) Wild, U.; Pfänder, N.; Schlägl, R. *Fresenius J. Anal. Chem.* **1997**, *357*, 420.
- (37) Sherwood, P. M. A. *J. Electron Spectrosc. Relat. Phenom.* **1996**, *81*, 319.
- (38) McFeely, F. R.; Kowalczyk, S. P.; Ley, L.; Cavell, R. G.; Pollak, R. A.; Shirley, D. A. *Phys. Rev. B* **1974**, *9*, 5268.
- (39) Desimoni, E.; Casella, G. I.; Morone, A.; Salvi, A. M. *Surf. Interface Anal.* **1990**, *15*, 627.
- (40) Desimoni, E.; Casella, G. I.; Salvi, A. M. *Carbon* **1992**, *30*, 521.
- (41) Arrigo, R.; Hävecker, M.; Wrabetz, S.; Blume, R.; Lerch, M.; McGregor, J.; Parrott, E. P.; Zeitler, J. A.; Gladden, L. F.; Knop-Gericke, A.; Schlägl, R.; Su, D. S. *J. Am. Chem. Soc.* **2010**, *132* (28), 9616–30.
- (42) Arrigo, R. Ph.D. Thesis, TU Berlin, 2009
- (43) Lahaye, J.; Nanse, G.; Fioux, P.; Bagreev, A.; Broshnik, A.; Strelko, V. *Appl. Surf. Sci.* **1999**, *147*, 153.
- (44) Pels, J. R.; Kapteijn, F.; Moulijn, J. A.; Zhu, Q.; Thomas, K. M. *Carbon* **1995**, *33*, 1641.
- (45) Seah, M. P.; Dench, W. A. *Surf. Interface Anal.* **1979**, *1*, 2–11.
- (46) Bluhm, H.; Havecker, M.; Knop-Gericke, A.; Kleimenov, E.; Schlägl, R.; Teschner, D.; Bukhtiarov, V. I.; Ogletree, D. F.; Salmeron, M. *J. Phys. Chem. B* **2004**, *108*, 14340–14347.
- (47) Zangwill, A. *Physics at Surfaces*; Cambridge University Press: New York, 1988.
- (48) Chiou, J. W.; Yueh, C. L.; Jan, J. C.; Tsai, H. M.; Pong, W. F.; Hong, I. H.; Klauser, R.; Tsai, M.-H. *Appl. Phys. Lett.* **2002**, *81*, 4189.
- (49) Waidmann, S.; Knupfer, M.; Fink, J.; Kleinsorge, B.; Robertson, J. *J. Appl. Phys.* **2001**, *89*, 3783.
- (50) Brandes, J. A.; Cody, G. D.; Rumble, D.; Haberstroh, P.; Wirick, S.; Gelinas, Y. *Carbon* **2008**, *46*, 1424.
- (51) Urquhart, S. G.; Hitchcock, A. P.; Priester, R. D.; Rightor, E. J. *J. Polym. Sci. Part B* **1995**, *33*, 1603.
- (52) Kuznetsova, A.; Popova, I.; Yates, J. T., Jr.; Bronikowski, M. J.; Huffman, C. B.; Liu, J.; Smalley, R. E.; Hwu, H. H.; Chen, J. G. *J. Am. Chem. Soc.* **2001**, *123*, 10699–10704.
- (53) Lenardi, C.; Pisenti, P.; Brizio, V.; Bottani, C. E.; Li Bassi, A.; Milani, P. *J. Appl. Phys.* **1999**, *85*, 7159.
- (54) Urquhart, S. G.; Ade, H. *J. Phys. Chem. B* **2002**, *106*, 8531.
- (55) Terminello, L. J.; Shuh, D. K.; Himpel, F. J.; Lapiano-Smith, D. A.; Stöhr, J.; Bethune, D. S.; Meijer, G. *Chem. Phys. Lett.* **1991**, *182*, 491.
- (56) Bressler, P. R.; Lübbe, M.; Zahn, D. R. T.; Braun, W. *J. Vac. Sci. Technol. A* **1997**, *15*, 2085.
- (57) Kikuma, J.; Yoneyama, K.; Nomura, M.; Konishi, T.; Hashimoto, T.; Mitsumoto, R.; Ohuchi, Y.; Seki, K. *J. Electron Spectrosc. Relat. Phenom.* **1998**, *88*–91, 919.
- (58) Fischer, D. A.; Wentzcovitch, R. M.; Carr, R. G.; Continenza, A.; Freeman, A. *J. Phys. Rev. B* **1991**, *44*, 1427.
- (59) Entani, S.; Ikeda, S.; Kiguchi, M.; Saiki, K.; Yoshikawa, G.; Nakai, I.; Kondoh, H.; Ohta, T. *Appl. Phys. Lett.* **2006**, *88*, 153126.
- (60) Batson, P. E. *Phys. Rev. B* **1993**, *48*, 2608.
- (61) Atamny, F.; Blöcker, J.; Henschke, B.; Schlägl, R.; Schedel-Niedrig, T.; Keil, M.; Bradshaw, A. M. *J. Phys. Chem.* **1992**, *96*, 4522.
- (62) Chen, P.; Wu, X.; Sun, X.; Lin, J.; Ji, W.; Tan, K. L. *Phys. Rev. Lett.* **1999**, *82*, 2548.
- (63) Proctor, A.; Sherwood, P. M. A. *J. Electron Spectrosc. Relat. Phenom.* **1982**, *27*, 39.
- (64) Proctor, A.; Sherwood, P. M. A. *Anal. Chem.* **1982**, *54*, 13.
- (65) Felicíssimo, V. C.; Cesar, A.; Luo, Y.; Gel'mukhanov, F.; Ågren, H. *J. Phys. Chem. A* **2005**, *109* (33), 7385.
- (66) Plashkevych, O.; Carravetta, V.; Vahtras, O.; Ågren, H. *Chem. Phys.* **1998**, *232*, 49.
- (67) Clark, D. T.; Thomas, H. R. *J. Polym. Sci.* **1976**, *14*, 1671.
- (68) Clark, D. T.; Peeling, J.; Cooling, L. *Biochim. Biophys. Acta* **1976**, *453*, 533.
- (69) Schedel-Niedrig, T.; Weiss, W.; Schlägl, R. *Phys. Rev. B* **1995**, *52*, 17449.
- (70) Dong, G. L.; Hüttlinger, K. J. *Carbon* **2002**, *40* (14), 2515–2528.